Journal of Magnetic Resonance 381 (2025) 107988

Contents lists available at ScienceDirect

Journal of Magnetic Resonance

journal homepage: www.elsevier.com/locate/jmr

Sample-accessible multi-resonance X-band EPR triple ring resonator

Chun Him Lee [a], Meltem Elitaş [a,b], Jan G. Korvink [a,*], Mazin Jouda [a,*]

[a] Institute of Microstructure Technology, Karlsruhe Institute of Technology, Eggenstein-Leopoldshafen, 76344, Germany
[b] Faculty of Engineering and Natural Sciences, Sabancı University, Istanbul, 34956, Turkiye

ARTICLE INFO

Dataset link: DOI: 10.35097/dzacz1fcgw7a5ee5

Keywords:
Parallel EPR
Sample-accessible
High-throughput

ABSTRACT

Micro-resonators downsize their resonating structures, reaching frequencies required for electron paramagnetic resonance (EPR) spectroscopy, thus allowing sensitive detection of mass-limited samples. Planar resonators provide accessibility of the sample space, allowing *in situ* and *operando* experiments for convenient characterization with access to environmental parameters such as UV radiation, gas and liquid flow, and better temperature gradient control. We report a novel triple-ring resonating structure that exploits the benefits of sample accessibility and its miniaturized structure. It offers three simultaneously operating X-band channels (8 GHz to 11 GHz) with a real-time accessible 50 nL sample volume for each channel, with a maximum spin sensitivity of 1.18×10^8 Spin/Hz$^{1/2}$. By cascading the ring resonators, we improve the quality factor of each resonance by reflecting and confining the electromagnetic energy by the neighboring rings. The Q-factor of the center resonance at 9.45 GHz with the enhancement of 2 passive reflectors reaches 73. Three relative translations allow a wide range of tuning, matching, suppressing, and isolating the resonances. While the introduced resonator exhibits three resonances only, it can be readily upscaled to feature more resonances, thus opening the door to high-throughput parallel EPR spectroscopy.

1. Introduction

Electron paramagnetic resonance (EPR) spectroscopy has emerged as a powerful tool for paramagnetic species studies in physics, chemistry, biology, medicine, and material science. It offers information about electronic structures, spin dynamics, and molecular interactions [1–4]. Over the years, several spectroscopic techniques have been developed over EPR, providing improvements in sensitivity [5], enabling long-range distance measurements between spin centers for molecular structure and conformation studies [6,7], enhancing the resolutions of hyperfine interactions to investigate nuclear-spin coupling [8], transferring electron spin magnetization to nuclear spins [9], studying transient dynamics of fast chemical processes [10], and target site analysis [11]. Despite these advances, studies have focused mainly on single-sample measurement, which makes EPR a low-throughput technique. This becomes more challenging for advanced experiments requiring real-time optical, electrical, mechanical, or chemical interactions.

In studies of catalysis, for instance, evaluating the catalyst material, associated radical species, and catalytic reactions is essential for understanding the underlying mechanisms. The limitations of sample access, operation temperature, and single-sample EPR spectroscopy impede catalytic experiments with different variables [12–15]. Sample-accessible multi-sample EPR spectroscopy increases throughput and accelerates screening under varying environmental conditions. One can actively monitor or modify the catalysis conditions throughout the experiment in real time, which enables a deeper understanding of transient reaction pathways. This advantage benefits not only catalysis studies, but also different disciplines in material research, quantum communication [16], and biomedicine [17].

In previous work, we reported a robust multi-sample ultra-high frequency (UHF) EPR spectroscopy scheme combining lock-in detection and decoupling of sample cells [18]. It reveals the possibility of high-throughput EPR spectroscopy. Building on this, we developed an X-band triple-resonance ring resonator, offering a single readout with potentially three samples simultaneously. Featuring a higher sensitivity, sample accessibility [19], and the possibility to integrate microfluidic channels [20], the triple-resonance detector offers high flexibility in experimental designs, especially for *in situ* catalysis and reaction monitoring. In addition to these features, the resonator was tested against a commercially available X-band high-Q EPR cavity. The results showed a comparable signal-to-noise ratio (SNR) for 1,3-bisdiphenylene-2-phenylallyl (BPDA). Two variants are proposed besides the original design, enhancing the geometrical selectivity of the multi-sample parallel readout.

* Corresponding authors.
E-mail addresses: jan.korvink@kit.edu (J.G. Korvink), mazin.jouda@kit.edu (M. Jouda).

https://doi.org/10.1016/j.jmr.2025.107988
Received 31 May 2025; Received in revised form 7 October 2025; Accepted 10 October 2025
Available online 14 October 2025

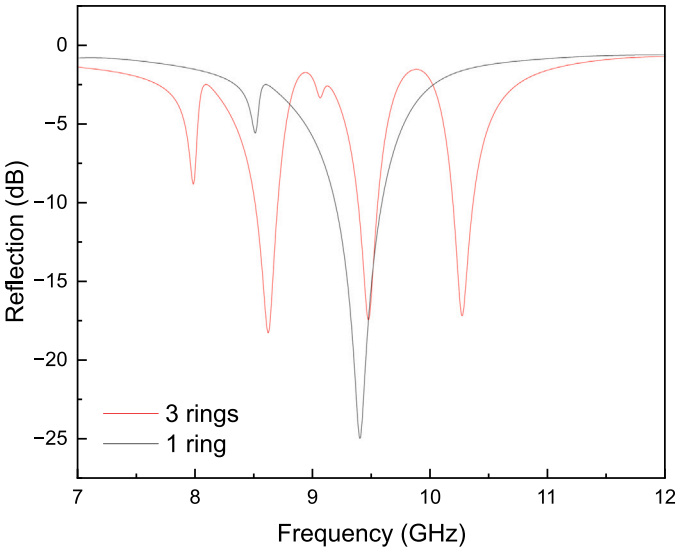

Fig. 1. Simulation of quality factor comparison of a one-ring resonator structure and a three-ring resonator structure in S_{11} curve, the quality factor increases in a three-ring structure due to the wave reflection by the neighboring rings.

2. Methods

2.1. Detector design

The triple-resonance ring resonator design follows a well-established ceramic printed circuit board (PCB) manufacturing process. Ceramic PCB is known for its high dielectric constant, low loss tangent, and high thermal conductivity. This material allows structure miniaturization, increasing sensitivity, and stabilizing the local temperature for EPR measurements because of rapid heat conduction and dissipation. Aluminum oxide, or Alumina (Al_2O_3), is a widely used ceramic material in various high-frequency disciplines due to the notable electrical, thermal, and mechanical properties [21], which are favorable for EPR spectroscopy. In addition, a mature production process lowers the production cost of the resulting chip.

Eq. (1) describes the behavior of a planar ring resonator, where f_0 is the resonance frequency, c is the speed of light, and r is the radius of the ring.

$$f_0 = \frac{c}{2\pi r\sqrt{\epsilon_{\text{eff}}}}. \tag{1}$$

The effective dielectric constant ϵ_{eff} of the substrate can be calculated using the equation [22],

$$\epsilon_{\text{eff}} = \frac{\epsilon_r + 1}{2} + \frac{\epsilon_r - 1}{2}\left(1 + \frac{12h}{w}\right)^{-\frac{1}{2}}, \tag{2}$$

where ϵ_r, h, and w are respectively the substrate's relative permittivity or dielectric constant, and the height and width of the trace [23]. For comparison, the dielectric constant of air is 1, whereas that of 96% Alumina is 9.4.

The resonance frequency of the center ring is set at 9.5 GHz. When the working frequency of the spectrometer is set to the center frequency, the inner and outer rings are inactive due to frequency mismatch. However, they reflect the propagating wave and conserve electromagnetic energy within the gap and the center ring, resulting in a higher Q-factor, as shown in Fig. 1. In addition, the inner and the outer rings act as resonators in a neighboring frequency, forming a triple resonant structure. In the current design, the width of the copper rings and their separation are set to 100 μm, with the radius of the center ring set to 2435 μm. The diameter of the circular substrate for the triple ring

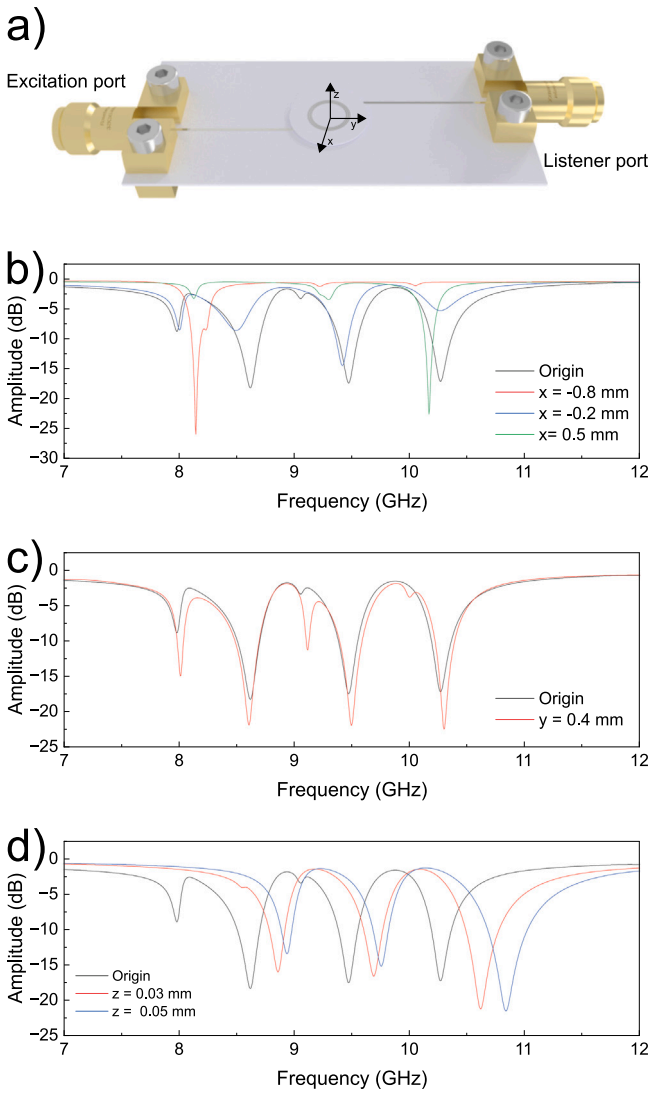

Fig. 2. (a). The three-dimensional tuning is achieved by relative translational movement of the triple-resonance ring with respect to the feedline. Measured changes in the S_{11} curve according to relative translations of the concentric resonator ring stack along the **(b)** x, **(c)** y, and **(d)** z axes. In EPR measurements using reflective spectroscopy, a microwave signal was injected from the excitation port, and the listener port was terminated by a 50 Ω load.

resonator 10 mm. This design combines the governing Eqs. (1) and (2), the manufacturing limit, and sufficient frequency separation among all resonances. Note that the matching and quality factor depend on the distance between the side and center rings. It depends additionally on the tuning conditions. For our proposed prototype, the design achieved a maximum Q-factor of 73 with a matching of −25 dB. The ring resonator was excited by placing it on top of a two-port feedline structure. The edge-launch feedlines are designed on a 48.5×21.8mm with an 50 Ω line impedance. The width and the length of the feedlines are 26.4 mm and 0.325 mm, respectively. Additionally, the feedlines are placed at an offset of 2.397 mm away from center on the opposite side. The feedline ends at the bottom of the substrate under the copper rings, which allows the ring resonator to be inductively coupled in the shortest distance.

Using a two-port system has the following advantages: it allows measurement of the EPR signal through reflection and transmission. Furthermore, it allows accessing the signals corresponding to the three resonances from the first, second port, or both [24,25]. By incorporating x- and y-offsets (Fig. 2 a) with a two-port system, we can

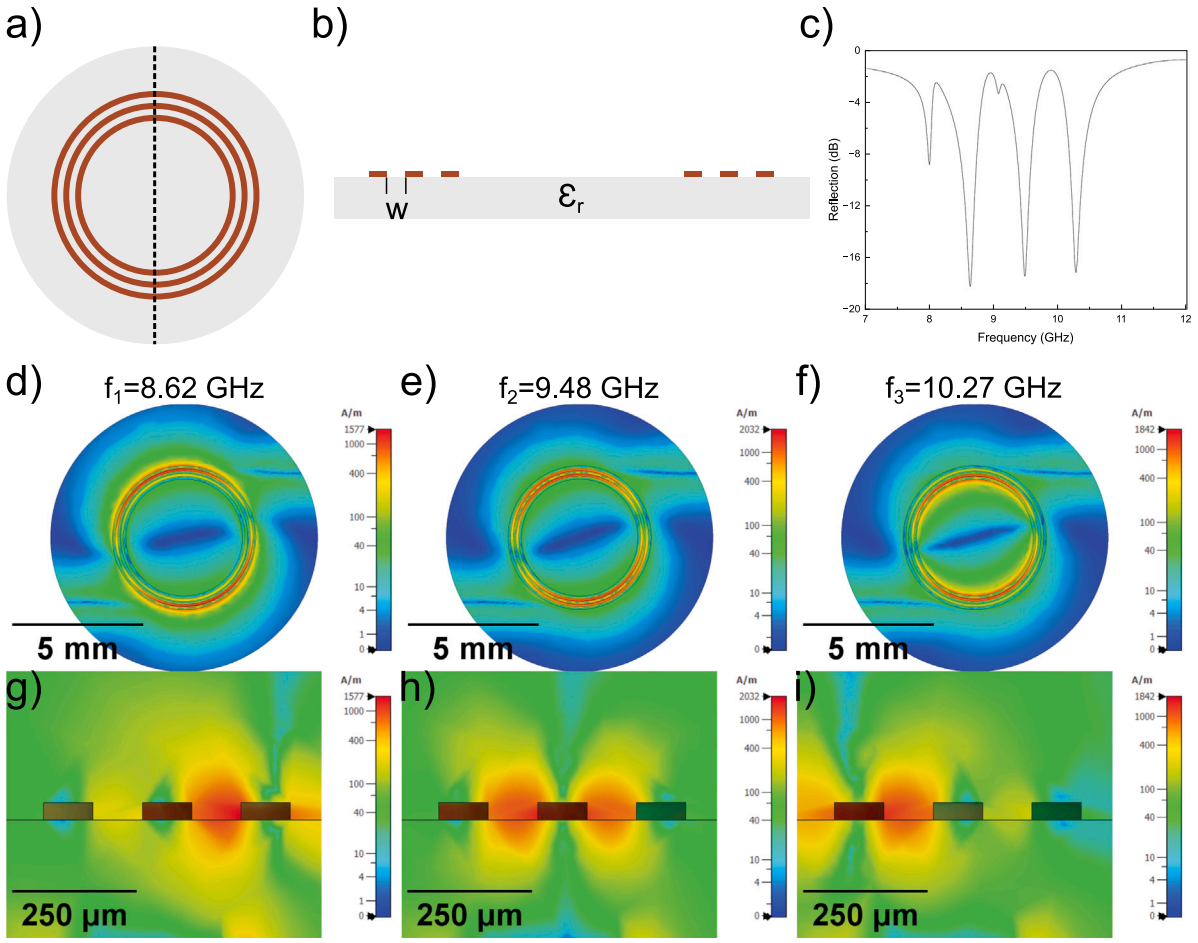

Fig. 3. The triple-resonance ring resonator with concentric topology and its H-field distributions. **(a)** Top and **(b)** cross-section views of the triple-resonance ring resonator with a concentric topology, w is the distance between two copper rings, ϵ_r is the dielectric constant of the substrate. **(c)** The S-parameter shows the three resonances at 8.62 GHz, 9.48 GHz, and 10.27 GHz. The respective top views of the H-field distributions are shown in **(d)**, **(e)**, and **(f)**, and their respective cross-section planes are in **(g)**, **(h)**, and **(i)**.

flexibly make one or more resonances highly detectable on one port. In contrast, nearly invisible on the other, or vice versa. Various instances are shown in the supplementary material Figure S.1. When the tuning and matching reach triple resonance at one port simultaneously, one can use a single microwave channel to acquire all three spectra simultaneously [18]. For reflection EPR spectroscopy, in which the reflection of the RF signal is measured, a 50 Ω load can be connected to the second port to complete the electrical pathway.

A finite element method electromagnetic solver (CST Studio Suite, Dassault Systèmes Simulia Corp.) models, verifies, and optimizes the design. The frequency domain solver with adaptive tetrahedral mesh refinement and open boundary is used for the S-parameter simulation. The input power is set to 500 mW, the frequency range is set to 7 GHz to 12 GHz, and the microstrip line port is defined using the embedded port extension calculator. Lastly, E-field and H-field monitors are set for each resonance.

Designing the triple-resonance ring resonator and the feedline independently allows three relative translational degrees of freedom for tuning and matching, the movement follows the Figs. 2 a. Since the position of the ring determines the coupling, moving the triple-resonance ring resonator serves to tune and match the resonance frequencies. These movements are typically in the range of 1 mm as shown in the simulation results of Fig. 2. After terminating the listener port with a 50 Ω load, the movements are described with respect to the excitation line so that the triple-resonance ring resonator operates in a reflective EPR mode on the excitation port.

For example, moving the resonator along the x-axis or perpendicular to the feedline can focus the outer and inner rings and suppress the other resonances since the other rings move further away from the feedline and decouple themselves. On the other hand, moving the resonator along the y-axis matches the disc, but also leads to the resonance of the feedline, hence causing side resonance. Finally, moving the resonator along the z-axis tunes the resonator. When placed in the center, three resonances will be matched simultaneously, allowing various samples to be put into three channels for parallel measurements.

As depicted in Fig. 2, when the resonator is placed off-center, it shifts and focuses on the low or high resonance. However, only when the resonator is placed in the center would the three resonances match up to −18 dB. When a single resonance is considered, the neighboring ring resonators are silenced, forming a coplanar waveguide. Figs. 3, 4, and 5 show CST Studio simulations of the H-field map along with the reflection curve of the ring resonator under different conditions. Fig. 3 shows that three resonances are equally matched when the resonator is placed in the center. When the disc is placed in the center with a zero z-offset, the field strength is at maximum, reaching 1516.23 A m^{-1} for 9.48 GHz. We can estimate the geometrical selectivity of the detector over different resonances by finding the quotient of the target response against the interferent response, as described by the following equation.

$$S_i = \frac{R_{\text{target}}}{R_{\text{target}} + R_{\text{interferent}}} = \frac{B^2_{1z(s_i,f_i)}}{\sum B^2_{1z(s_n,f_i)}} \tag{3}$$

A maximum of two interference sources from two other resonances would exist in a triple-resonance system. From Fig. 3, we can calculate

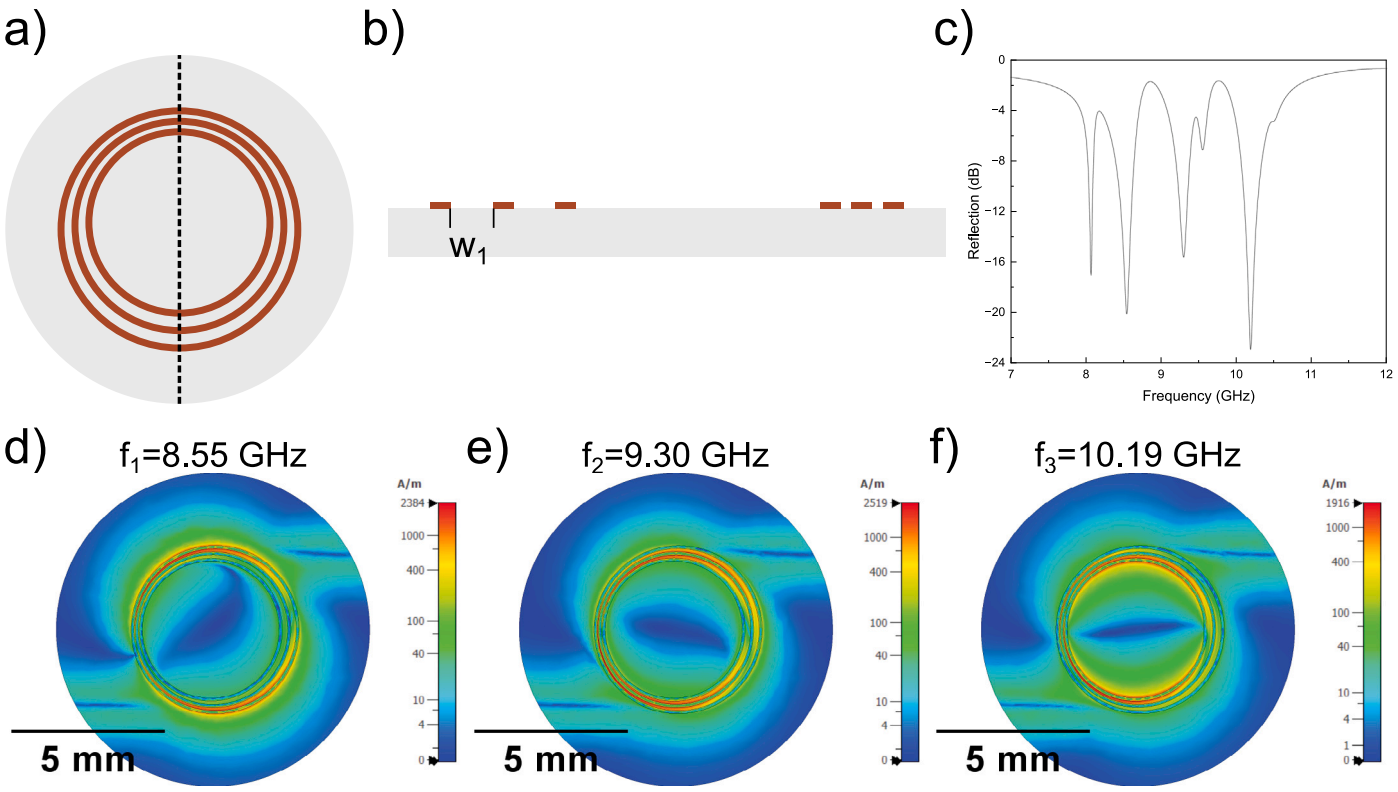

Fig. 4. The triple-resonance ring resonator with an eccentric topology and its H-field distributions. **(a)**Top and **(b)** cross-section views of the triple-resonance ring resonator with an eccentric topology, w_1 is the distance between the two copper rings. **(c)** The S-parameter shows the three resonances at 8.55 GHz, 9.30 GHz, and 10.19 GHz. The respective top views of the H-field distributions are shown in **(d)**, **(e)**, and **(f)**.

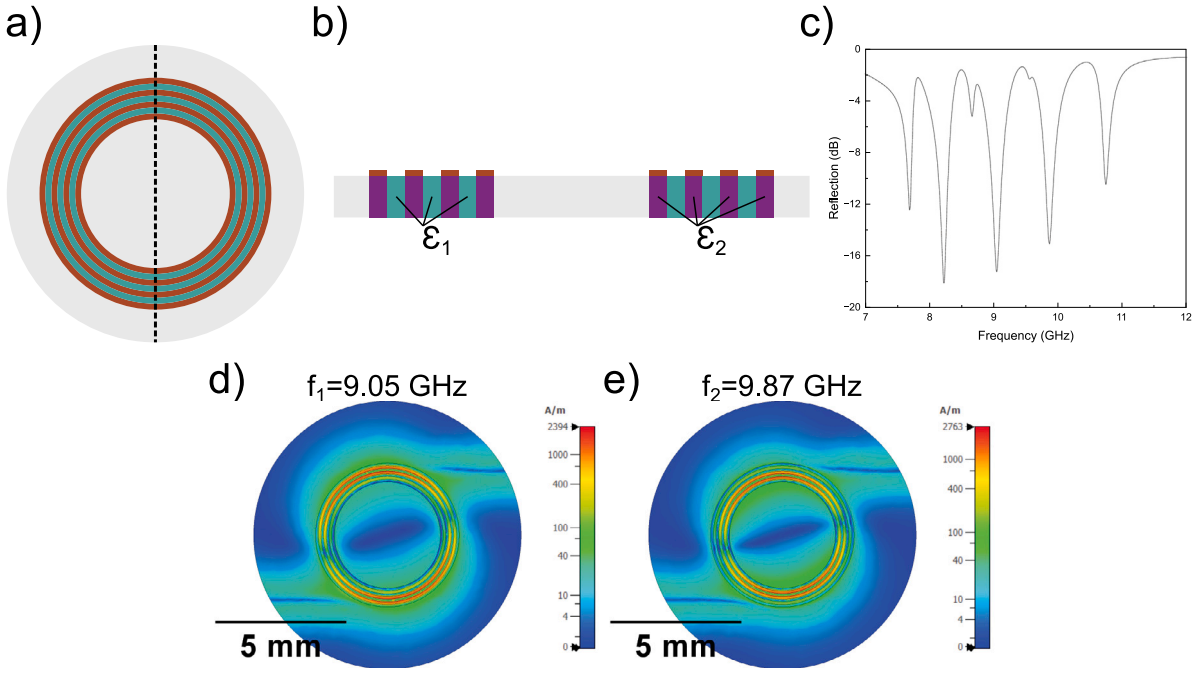

Fig. 5. The triple-resonance ring resonator on a substrate with a varying dielectric constant and its H-field distributions. **(a)**Top and **(b)** cross-section views of the triple-resonance ring resonator with an epsilon varying (ϵ_1, ϵ_2) substrate. **(c)** The S-parameter shows two resonances at 9.05 GHz, 9.87 GHz operating in the independent channels. The respective top views of the H-field distributions are **(d)**, and **(e)**.

that the respective optimal geometrical selectivity for resonance at 8.62 GHz, 9.48 GHz, and 10.27 GHz are 84%, 99%, and 29%. In other words, when reading the spectrum at center resonance, 1% of the signal due to other resonances is detectable. Various designs have been simulated to showcase the potential to improve the overall geometrical selectivity of the schemes when we loosen the design restriction. The prototype provides an enhanced Q-factor in the primary resonance in the center ring, and the secondary resonances are set to complement

the coplanar waveguide for the center resonance. Setting the ring resonators in an eccentric topology causes a phase shift and dephases the magnetic field maxima of all resonances. Figures S.2 and Table S.1 in the supplementary material summarize the sensitivity per resonance and geometrical selectivity under different sample positioning scenarios. From Fig. 4, when the magnetic field strength is monitored on the plane perpendicular to the feedline direction (xz-plane) and 750 μm, the optimal geometrical selectivity for the resonances at 8.55 GHz, 9.30 GHz, and 10.19 GHz is 94%, 99%, and 52%. Similarly, by varying the dielectric constant of the substrate in different regions, we can manipulate the wave propagation ($\lambda = c_0/(f\sqrt{\epsilon_r})$) of the three resonances and create a region where the magnetic field is better isolated from other resonance frequencies. For instance, increasing the dielectric constant of the substrate under the copper ring to 14.4 while decreasing it under the gap to 8.4 changes the wave propagation in the substrate and free space, resulting in a 30 MHz bandwidth enhancement of the center resonance and foster the wave attenuation in free space. An additional ring can be added, forming three sample channels. Additionally, one can abandon the center channel to increase the geometrical selectivity further and isolate the sample region. As seen in Fig. 5, the optimal geometrical selectivity for the resonance at 9.05 GHz and 9.87 GHz changes to 97% and 97%, respectively.

Going through geometrical and material design can substantially improve the geometrical selectivity of the triple-resonance ring resonator. To benefit from the maximum sensitivity of the resonator, one should also consider the maxima of the resonator along the angular position of the copper ring and the distance between the sample and the ring resonator of the desired readout frequency. As it has a noticeable effect on the H-field, as shown in the top view of the H-field in Figs. 3, 4, and 5. To calculate the optimal position for placing the sample, one can divide the ring resonator into 360 radial slices and estimate the H-field profile in each slice. For our fabricated design, the optimal sample location is when ϕ, the angle with respect to the excitation, is equal to 29°. Figures S.3, S.4, S.5, S.6 show the H-field profile characterizations against the slices and radial position to the center.

2.2. Manufacturing

The design was fabricated by a ceramic PCB manufacturer (RayMingPCB). Both structures were manufactured in 96% Alumina with copper metalization and non-magnetic immersion silver as oxidation protection. The substrate thicknesses of the feedline and the triple-resonance ring resonator are 381 μm and 254 μm, respectively. The manufacturing procedure is described as follows: the alumina powder was mixed with binders and sintering aids to form a slurry and cast into sheets of green tape. Copper deposition or lithography happened after the formation of the green tape. The board underwent a low-temperature firing process (500 °C to 1000 °C) to remove any binders and organic compounds and further sintered at high temperature (1600 °C) to compact the ceramic particles and form bonds between conductive layers and ceramic panels, resulted in a height of 35 μm for the conductive copper trace. Holes were created with a laser or mechanical drill in the stage, with plated vias being deposited during the green tape formation. A thin silver layer was electroplated on the conductive paths to protect the copper from oxidation.

Using in-house postprocessing, atomic layer deposition (ALD) was performed to isolate the copper rings and prevent corrosion, especially for liquid-state samples. We used $TiCl_4$ and H_2O as precursors in the ALD system (Picosun R-200 ALD, SiSTEM technology). 220 cycles were performed at 100 °C and purged between the precursor pulses with nitrogen to achieve a 10 nm thick TiO_2 layer.

2.3. EPR setup

A screw-down edge-launch SMA connector (32K243-40ML5, Rosenberger Hochfrequenztechnik) connected the feedline to the spectrometer with a WR-90 to SMA converter (PE9804, Pasternak Enterprises) for the EPR experiment with ELEXSYS-II E500 to characterize the performance against the original cavity ELEXSYS Super High Sensitivity Probehead (Bruker BioSpin). On the other hand, an SMA cable was connected to a home-built wideband spectrometer to enable the readout of the three resonances. 1,3-bisdiphenylene-2-phenylallyl (BPDA) was used to characterize the detector because it is known for a strong one-line spectrum with a linewidth of 1 G. The same amount of BDPA was applied to the triple-resonance ring resonator and the ELEXSYS Super High Sensitivity Probehead (ER4122SHQE, Bruker BioSpin). In addition, ((2,2,6,6-Tetramethylpiperidin-1-yl)oxyl, TEMPO) dissolved in ethanol was used to test the detector under a liquid-state sample.

Fig. 6 illustrates the experiment for the triple-resonance ring detection. To measure the SNR of the detector, the detector was connected directly to the EPR spectrometer along with a home-built Helmholtz coil, which generates a modulation field of 1 G at 100 kHz. Similarly, volume-controlled liquid-state samples were applied on top of the active region of the ring.

To acquire signals for the three resonances of the ring resonator, the spectrometer must provide a detection range between 8 GHz and 11 GHz. Measurement with the X-band EPR spectrometer (ELEXSYS-II E500 CW-EPR spectrometer, Bruker BioSpin) would not be sufficient due to the narrow detection range of 9 GHz to 9.9 GHz. Therefore, a home-built EPR spectrometer depicted in Fig. 6 was built to measure all resonances of the detector.

The spectrometer began from the microwave source, a Ka-band oscillator (8350B Sweep Oscillator, Hewlett-Packard) that is capable of sweeping the output power from −5 dBm to −20 dBm, and the frequency from 0.01 GHz to 26.5 GHz with a frequency sweep span from 50 ms to 1000 ms. With the flexibility provided by the microwave signal generator, the signal could be transmitted directly to the sample to precisely control the microwave power experienced by the sample, where a circulator (PE83CR000, Pasternack Enterprises) blocks the feedback to the microwave source. A zero-offset Schottky diode (PE8014, Pasternack Enterprises) detects the microwave power and outputs a DC signal, which can be monitored with low-frequency electronics. On the other arm, a reference signal was constructed and combined with the detector signal with splitters (11667B, Hewlett-Packard). The reference arm was controlled with a variable attenuator (AF766H-20, Advanced Technical Materials) and a phase shifter (LS-0121-1121, Spectrum Electrotechnik). The home-built X-band spectrometer was connected to the triple-resonance ring detector. The readout and signal were synchronized with the 600 MHz UHF lock-in amplifier (UHFLI, Zurich Instruments) and monitored with the vendor control software (LabOne, Zurich Instruments).

3. Results

3.1. S-parameter measurement

An S-parameters measurement was conducted to characterize the chip's performance and verify that the fabrication was consistent with the simulation. The reflection of the triple-resonance ring resonator was measured by connecting one end of the resonator to the 26.5 GHz handheld microwave analyzer (N9918 A FieldFox, Keysight) while terminating the other end with a 50 Ω load. Fig. 7 shows the measurement of the fabricated structure against a simulation instance where the disc was shifted vertically along the microstrip line. In this case, the disc was shifted 0.6 mm away from the active port. We observed from the simulation that when the ring resonator is coupled to the microstrip line and resonates at 8.62 GHz, 9.50 GHz, 10.30 GHz, the microstrip line itself oscillates and generates a secondary resonance at 8.01 GHz, 9.13 GHz,

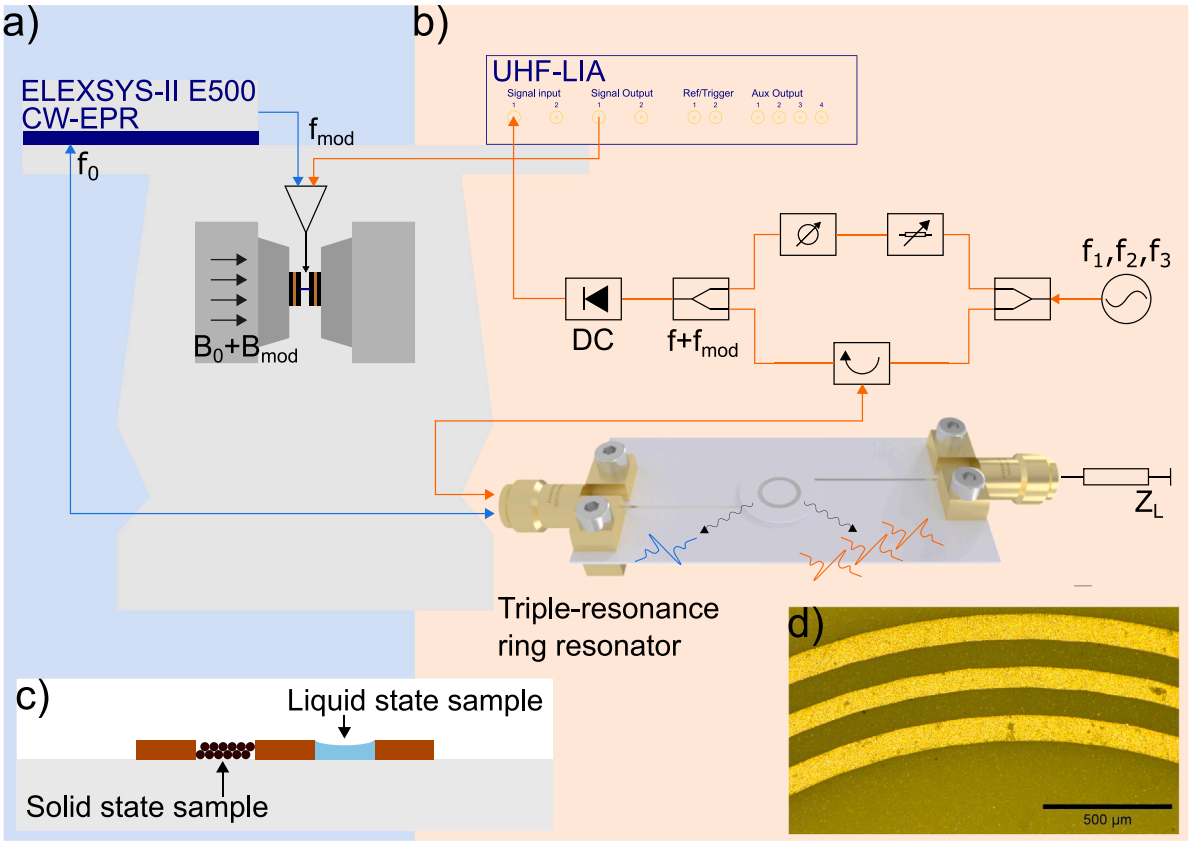

Fig. 6. The EPR measurement setup of the triple-resonance ring resonator. Two different setups are illustrated for the experiment **(a)** ELESYS-II E500 CW-EPR setup integration and **(b)** home-built EPR spectrometer that generates and reads the EPR spectrum across the three resonances of the resonator. f is the microwave frequency and B stands for the microwave magnetic field at Larmor frequency f_{Larmor}. **(c)** Illustration of the solid and liquid sample placement on the triple-resonance ring resonator. **(d)** Microscope picture of the triple-resonance ring resonator. The copper rings are in yellow, the scale bar is 500 µm.

10.01 GHz. The side resonance persisted in the fabricated structure with a less pronounced profile. On the other hand, the resonances in the ring resonator occurred at 8.30 GHz, 9.58 GHz, 10.37 GHz. Resulting in a frequency shift of 0.32 GHz, 0.08 GHz, 0.07 GHz. The differences between the matching also highlighted the manufacturing discrepancies. The ring resonator in Fig. 6 d was measured with a digital microscope (VHX600, Keyence). The radius of the fabricated center ring was 2.416 mm, and the width of the three rings from low to high resonance were 95.98 µm, 64.00 µm, and 124.84 µm, respectively. And the gap between the corresponding rings were 132.43 µm and 102.92 µm, respectively. A comparison between the measured dimensions and simulation can be found in Figure S.7. Nevertheless, the measurements showed a high resemblance to the simulations with all resonances achieving a matching better than −18.74 dB.

3.2. EPR measurements

After the S-parameters characterization, all resonances represented by different rings are equally matched, and the microwave frequency is set to the center frequency and the microwave power is set to 2 mW, accessible by the ELEXSYS-II E500 microwave bridge. BDPA was applied onto the copper rings of the resonator, and the resonator was positioned in the center of the ELEXSYS-II E500 magnet along with a home-built modulation coil. After that, an EPR spectroscopy experiment was performed at the center resonance of the triple-resonance ring resonator. After the measurement, the BDPA was retrieved and put in a 5 mm EPR tube, and once again measured under the default setup. Fig. 8 shows the SNR between the triple-resonance ring resonator and the ER4122SHQE. The recorded peak-to-peak SNR was 36134 and 54441,

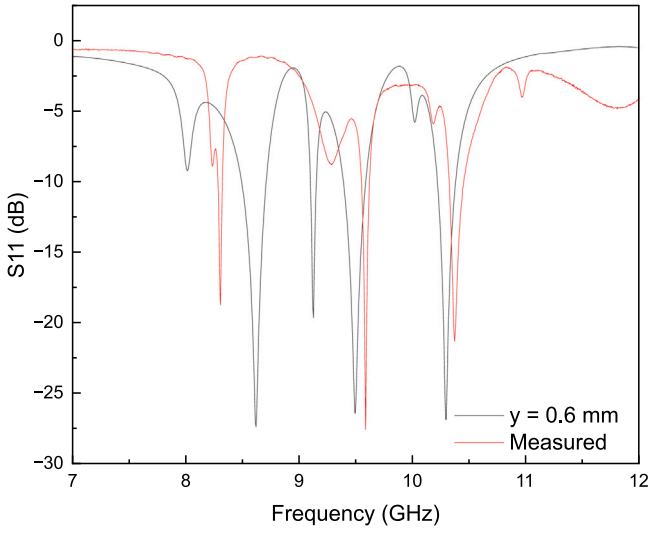

Fig. 7. S_{11} curves of the experimental (red) and simulated (black) S_{11} when the triple-resonance ring resonator was placed at 600 µm offsets parallel and away from the excitation port.

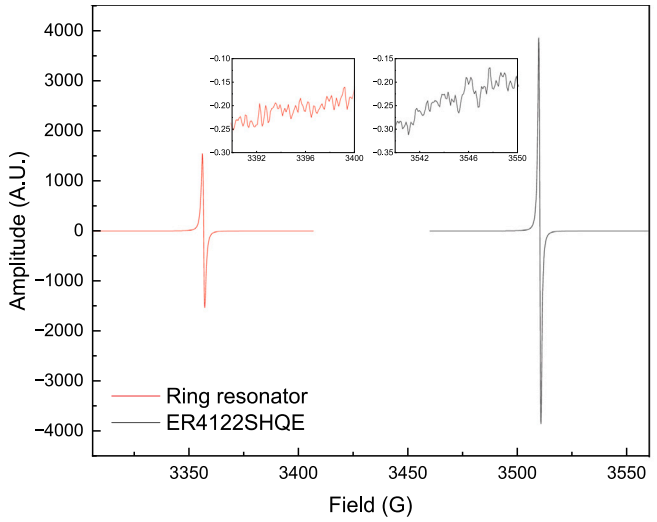

Fig. 8. BDPA EPR spectrum measured with the center frequency of the triple-resonance ring (red) and the ELEXSYS Super High Sensitivity Probehead ER4122SHQE (black). The microwave frequency for the ring resonator is set to the center resonance. In both cases, the same sample volume was used. The inserted graph shows the amplitude of noise.

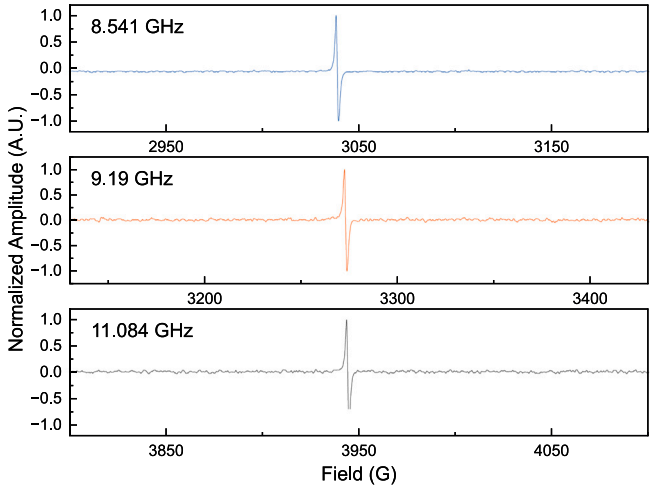

Fig. 9. Measurements of BDPA at all of the resonances of the triple-resonance ring resonator with a home-built X-band EPR spectrometer.

respectively. We can calculate the theoretical SNR and spin sensitivity described in [26].

$$\mathrm{SNR} = \frac{S_{max}}{3N_{RMS}} = \frac{(\gamma B_1 M_0)\left(\frac{B_0}{\Delta B}\right)B_u V}{3\sqrt{4kTR\Delta f}} \tag{4}$$

Where in the quasi-ready and non-saturation state, the maximum absorption is dependent on the static magnetization M_0, applied radio frequency as magnetic field B_1, applied static magnetic field B_0, sample volume V, the localized magnetic field produced by unitary direct current carried by micro coil $B_u = B_1/I$, and the half-width at half maximum of the resonance ΔB. The thermal noise is related to temperature T, electrical resistance R, and noise bandwidth of the detection electronics Δf. Assuming the homogeneously broadened lines with relaxation times $T_1 \cong T_2$ where the RF magnetic field can be increased up to a value equal to the resonance line width without significant line broadening, the spin sensitivity was defined as,

$$N_{min} = \frac{1}{\mathrm{SNR}}\frac{NV}{\sqrt{\Delta f}} = \alpha\frac{T^{3/2}\sqrt{R}}{B_u B_0^2}\left[\mathrm{Spins\ Hz^{-1/2}}\right], \tag{5}$$

where $\alpha = (24k^{3/2}\gamma^{-3}\hbar^{-2}) \cong 20\ \mathrm{m^{-1}kg^{5/2}s^{-4}K^{-3/2}A^{-3}}$. To evaluate the performance of the ring's additional resonances, we connected the home-built broadband spectrometer to the triple-resonance ring resonator and conducted EPR spectroscopy sequentially. Utilizing a single microwave channel simplifies the overall circuit design. However, if the microwave generator can produce a signal comprising three distinct frequency components, it would be possible to acquire EPR signals from all three resonances simultaneously, following the approach described in [18]. In this experiment, BDPA was applied to the region of interest to ensure that the B_1 fields associated with each resonance effectively interacted with the sample spins during measurement. As shown in Fig. 9, the three resonances exhibited comparable performance, with signal-to-noise ratios (SNRs) of 50.6, 22.1, and 35.9, respectively. The observed differences in SNR between the home-built spectrometer and the ELEXSYS-II E500 system are likely attributed to the suboptimal biasing of the diode detector's current in the reference arm. This limitation stems from the use of mechanical variable phase shifters and attenuators, which restrict the precision of adjustment. Table 1 summarizes the characterization results of the resonator.

Table 1
Measured and simulated resonances, Q-factor, theoretical sensitivity factor, and spin sensitivity [26].

Description [unit]	f_1	f_2	f_3
Simulated resonance [GHz]	8.62	9.48	10.27
Measured resonance [GHz]	9.03	9.58	10.37
Simulated Q-factor	17.68	26.75	24.37
Measured Q-factor	87.47	23.95	31.90
Maximum spin sensitivity [10^8 Spin/Hz$^{1/2}$]	1.89	1.38	1.18
Average spin sensitivity [10^8 Spin/Hz$^{1/2}$]	8.91	4.62	5.07

The performance of the triple-resonance ring was evaluated using a liquid-state sample. A 5 μL volume of 10 mmol TEMPO dissolved in ethanol was introduced to the resonator. The resulting single-shot spectrum from this measurement is presented in Fig. 10.

Furthermore, a BDPA crystal is placed in various locations according to Figure S.2 to experimentally assess the crosstalk between the channels. Fig. 11 shows that only when the BDPA crystal is placed at the active sample region will the readout be sensitive. In this case, the spectrometer frequency was set to the resonance frequency of the center ring, and an EPR signal was recorded from the BDPA crystal as it is positioned at the sensitive region of each ring. The excitation microwave power was set to 2 mW. The figure shows a peak-to-peak signal of 7.6 when the sample is placed at the sensitive region of the center ring, while peak-to-peak signals of 0.14 and 0.39 were observed when the sample is placed at s1 and s3, respectively, reflecting an s1-s2 crosstalk of 1.8 % and an s2-s3 crosstalk of 5.1 %.

Lastly, a microwave power saturation experiment is performed to determine the linear regime of the triple-resonance ring resonator against the ELEXSYS Super High Sensitivity Probehead ER4122SHQE, as shown in Fig. 12.

4. Conclusion

4.1. Broadband adaptation of cascaded ring resonator

We reported a triple-resonance ring resonator that allows the simultaneous EPR measurement of three samples. The triple-resonance ring features a planar topology, offering apparent sample accessibility. The concentrically cascaded ring resonator forms a sample channel for a 50 nL liquid-state sample. The tuning and matching of the resonator are performed manually via sub-millimeter translational adjustments

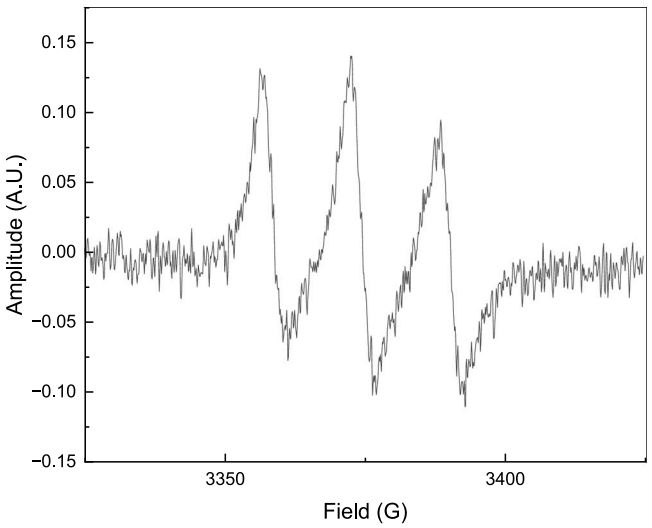

Fig. 10. A single shot measurement of a 5 μL sample made up of from 10 mmol solution of TEMPO dissolved in ethanol. The sample is applied and spread across the detector.

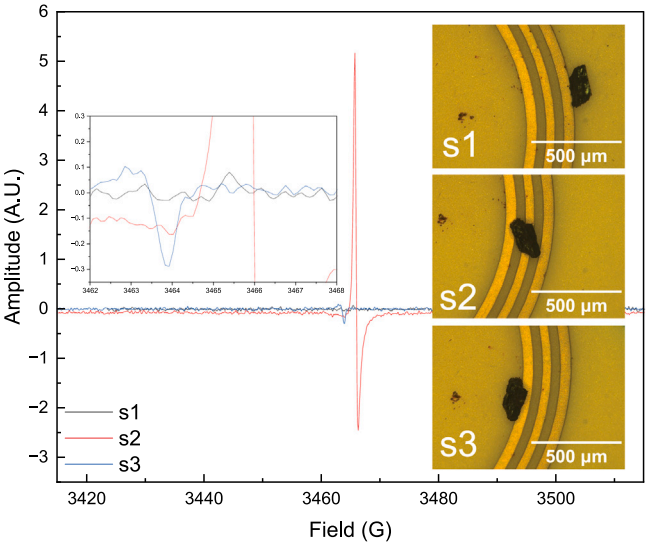

Fig. 11. Crosstalk measurements where the same BDPA crystal is placed in s_1, s_2, and s_3 according to Figure S.2 c. The microwave frequency for the ring resonator is set to the center resonance.

along three axes. This setup provides broad and flexible tunability, enabling both reflection and transmission EPR measurements at one, two, or all resonances, in any desired combination. While manual tuning was used in this study, the tuning and matching process can be readily automated, such as with piezoelectric or linear actuators, to achieve more precise and reproducible control. The measurement showed a maximum Q-factor of 73 and maximum spin sensitivity of 1.18×10^8 Spin/Hz$^{1/2}$ when the ring resonator is tuned to an optimal position and the sample is applied at the maximum field profile described at 29°. The average spin sensitivity across different radial angles of the resonator is 4.62×10^8 Spin/Hz$^{1/2}$. Moreover, the simulation results highlighted the potential for enhancing resonance selectivity and sensitivity by optimizing the resonator's topology and material. Integrating the proposed resonator with the broadband excitation and acquisition approach described in [27,28] enables broadband EPR while preserving the sensitivity provided by resonance.

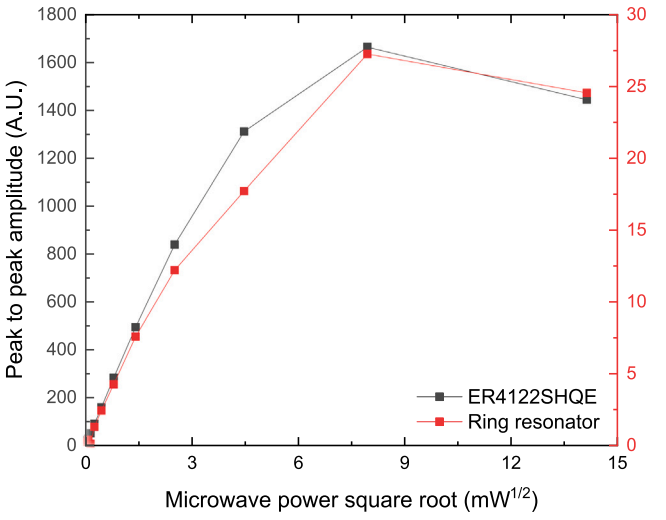

Fig. 12. EPR microwave power saturation curve comparison for the triple-resonance ring (red) and the ELEXSYS Super High Sensitivity Probehead ER4122SHQE (black). In both cases, the sample shown in Fig. 11 is used.

Previous studies have explored various strategies to enhance EPR performance. For example, Narkowicz et al. [29] demonstrated that downsizing and miniaturizing EPR resonator structures can substantially improve microwave power conversion efficiency and detector sensitivity. Similarly, Dayan et al. [30] highlighted the combined benefits of miniaturization and cryocooling for further sensitivity enhancement. In another approach, Joshi et al. [31] showed that exploiting resonator harmonics enables EPR spectroscopy over an exceptionally wide frequency range, facilitating the separation of hyperfine and spin–orbit interactions in organic semiconductors. Additionally, Hagen et al. [32] reported the development of a broadband EPR resonator capable of operating across a large frequency span. In contrast to these efforts, our work focuses on realizing a multi-resonance structure that enables simultaneous measurements of different samples. Our triple-resonance design can also readily incorporate miniaturization techniques [29] or cryocooling [30] to boost sensitivity, and it could leverage the harmonic-based approach in [31] to perform parallel EPR at the harmonics of its three resonances.

4.2. Topology optimization

The triple-resonance ring resonator exhibits excellent potential in parallelizing X-band EPR spectroscopy, yet isolating regions of high electric and magnetic field intensity remains difficult. Recent developments in topology optimization provide computationally efficient and precise algorithms for intricate structures across different disciplines. The material allocation of the resonator can be enhanced through topology optimizations, allowing the simulator to precisely adjust the resonance frequencies, quality factors, and field distribution of a resonator [33–35]. This automated optimization approach simplifies the design process and reduces the necessity for manual modifications, iterative optimization, and extensive prototyping.

4.3. Mass-limited sample measurements

Treating the surface of the triple-resonance ring detector with an ultrathin ALD process isolates the liquid samples from the metal structure using a suitable dielectric, which enables the integration of microfluidic systems into our experimental setup. We could combine the resonator ring with a microfluidic well to conduct real-time EPR spectroscopy on limited volumes (nanoliter or subnano-liter volume) of precious or irreplaceable samples [20]. In addition, high-throughput EPR spectroscopy

could be integrated with microfluidic droplet generators [36] and could be utilized for pharmaceutical applications such as characterizing drugs or free radicals formed from drug sterilization procedures [37].

4.4. Background consistent and multi field comparative experiments

Parallelizing EPR spectroscopy in a geometrical- and frequency-selective resonator allows direct comparison of experimental sets, where parameters are altered and compared with a control spectrum. With sample accessibility, one can set up photo-catalytic experiments and cover one or more detection channels to perform light and dark experiments simultaneously [19,38]. Moreover, a catalyst can be fed through one or more microfluidic channels [39,40] to perform *in situ* and *operando* experiments to monitor the radical formation, or reaction kinetics and pathways. Such a setup could also be adopted for broadband multi-field NV center studies [41].

CRediT authorship contribution statement

Chun Him Lee: Writing – review & editing, Writing – original draft, Validation, Investigation, Data curation. **Meltem Elitaş:** Writing – review & editing, Resources, Investigation. **Jan G. Korvink:** Writing – review & editing, Supervision, Project administration, Funding acquisition, Conceptualization. **Mazin Jouda:** Writing – review & editing, Supervision, Methodology, Investigation, Conceptualization.

Declaration of competing interest

The authors declare the following financial interests/personal relationships which may be considered as potential competing interests: Jan G. Korvink reports a relationship with Voxalytic GmbH that includes: board membership.

Acknowledgments

Chun Him Lee, Jan G. Korvink, and Mazin Jouda were supported by the Deutsche Forschungsgemeinschaft (DFG, German Research Foundation) - SFB 1527/1 – project-ID 454252029 (HyPERiON). Additional support was provided by the Helmholtz Association Research Area Information, Materials Systems Engineering, Topic 5 Materials Information Discovery, by the CRC 1537 ECOSENSE, the ERC SygG HiSCORE, Karlsruhe Nano Micro Facility (KNMFi), and the Karlsruhe Institute of Technology. Meltem Elitaş acknowledges support from the Humboldt Foundation. Chun Him Lee acknowledges the Karlsruhe School for Optics and Photonics (KSOP) support. All authors sincerely thank Judith Hohmann for performing ALD. All authors acknowledge support from the Open Access KIT Publication Fund, enabled by Project DEAL.

Appendix A. Supplementary data

Supplementary material related to this article can be found online at https://doi.org/10.1016/j.jmr.2025.107988.

Data availability

Data will be made available on request or can be accessed under DOI:10.35097/dzacz1fcgw7a5ee5.

References

[1] J.A. Weil, J.R. Bolton, Electron Paramagnetic Resonance: Elementary Theory and Practical Applications, John Wiley & Sons, 2007.
[2] A. Schweiger, G. Jeschke, Principles of Pulse Electron Paramagnetic Resonance, Oxford University Press, 2001.
[3] G.R. Eaton, S.S. Eaton, Foundations of Modern EPR, World Scientific, 1998.
[4] D. Goldfarb, S. Stoll, EPR Spectroscopy: Fundamentals and Methods, John Wiley & Sons, 2018.
[5] R. Narkowicz, H. Ogata, E. Reijerse, D. Suter, A cryogenic receiver for EPR, J. Magn. Reson. 237 (2013) 79–84.
[6] T. Schmidt, M.A. Wälti, J.L. Baber, E.J. Hustedt, G.M. Clore, Long distance measurements up to 160 åin the groel tetradecamer using Q-band DEER EPR spectroscopy, Angew. Chem. Int. Ed. 55 (51) (2016) 15905–15909.
[7] Y.D. Tsvetkov, A.D. Milov, A.G. Maryasov, Pulsed electron–electron double resonance (PELDOR) as EPR spectroscopy in nanometre range, Russ. Chem. Rev. 77 (6) (2008) 487.
[8] W. Mims, Pulsed ENDOR experiments, Proc. R. Soc. Lond. Ser. A. Math. Phys. Sci. 283 (1395) (1965) 452–457.
[9] M. Abraham, M. McCausland, F. Robinson, Dynamic nuclear polarization, Phys. Rev. Lett. 2 (11) (1959) 449.
[10] K. Ishii, Y. Hirose, H. Fujitsuka, O. Ito, N. Kobayashi, Time-resolved EPR, fluorescence, and transient absorption studies on phthalocyaninatosilicon covalently linked to one or two TEMPO radicals, J. Am. Chem. Soc. 123 (4) (2001) 702–708.
[11] A. Kavalenka, I. Urbančič, V. Belle, S. Rouger, S. Costanzo, S. Kure, A. Fournel, S. Longhi, B. Guigliarelli, J. Strancar, Conformational analysis of the partially disordered measles virus NTAIL-XD complex by SDSL EPR spectroscopy, Biophys. J. 98 (6) (2010) 1055–1064.
[12] A. Brückner, In situ electron paramagnetic resonance: a unique tool for analyzing structure–reactivity relationships in heterogeneous catalysis, Chem. Soc. Rev. 39 (12) (2010) 4673–4684.
[13] H. Issa Hamoud, L. Wolski, I. Pankin, M.A. Bañares, M. Daturi, M. El-Roz, In situ and operando spectroscopies in photocatalysis: Powerful techniques for a better understanding of the performance and the reaction mechanism, Top. Curr. Chem. 380 (5) (2022) 37.
[14] M. Hunger, J. Weitkamp, In situ IR, NMR, EPR, and UV/Vis spectroscopy: Tools for new insight into the mechanisms of heterogeneous catalysis, Angew. Chem. Int. Ed. 40 (16) (2001) 2954–2971.
[15] M.M. Roessler, E. Salvadori, Principles and applications of EPR spectroscopy in the chemical sciences, Chem. Soc. Rev. 47 (8) (2018) 2534–2553.
[16] K. Sato, S. Nakazawa, S. Nishida, R.D. Rahimi, T. Yoshino, Y. Morita, K. Toyota, D. Shiomi, M. Kitagawa, T. Takui, Novel applications of ESR/EPR: quantum computing/quantum information processing, in: EPR of Free Radicals in Solids II: Trends in Methods and Applications, Springer, 2012, pp. 163–204.
[17] H.M. Swartz, N. Khan, J. Buckey, R. Comi, L. Gould, O. Grinberg, A. Hartford, H. Hopf, H. Hou, E. Hug, et al., Clinical applications of EPR: overview and perspectives, NMR Biomed. 17 (5) (2004) 335–351.
[18] C.H. Lee, J.G. Korvink, M. Jouda, Frequency multiplexing enables parallel multi-sample EPR, Sci. Rep. 14 (1) (2024) 11815.
[19] C. Mendoza, A. Désert, L. Khrouz, C.A. Páez, S. Parola, B. Heinrichs, Heterogeneous singlet oxygen generation: in-operando visible light EPR spectroscopy, Environ. Sci. Pollut. Res. 28 (2021) 25124–25129.
[20] N. Abhyankar, M.A. Catterton, G.A. Cooksey, V.A. Szalai, Microfluidic-integrated chip resonators for electron spin sensing in submicromolar, submicroliter solutions, Anal. Chem. (2024).
[21] M.T. Sebastian, H. Jantunen, Low loss dielectric materials for LTCC applications: a review, Int. Mater. Rev. 53 (2) (2008) 57–90.
[22] N.M. Shebani, A.E. Mohammed, B.M. Khamoudi, Design curves of microstrip ring resonator, in: 12th International Conference on Sciences and Techniques of Automatic Control & Computer Engineering December, 2011, pp. 18–20.
[23] D.M. Pozar, Microwave Engineering: Theory and Techniques, John Wiley & Sons, 2021.
[24] P.R. Shrestha, N. Abhyankar, M.A. Anders, K.P. Cheung, R. Gougelet, J.T. Ryan, V. Szalai, J.P. Campbell, Nonresonant transmission line probe for sensitive interferometric electron spin resonance detection, Anal. Chem. 91 (17) (2019) 11108–11115.
[25] N. Abhyankar, A. Agrawal, J. Campbell, T. Maly, P. Shrestha, V. Szalai, Recent advances in microresonators and supporting instrumentation for electron paramagnetic resonance spectroscopy, Rev. Sci. Instrum. 93 (10) (2022).
[26] G. Boero, M. Bouterfas, C. Massin, F. Vincent, P.-A. Besse, R. Popovic, A. Schweiger, Electron-spin resonance probe based on a 100 μm planar microcoil, Rev. Sci. Instrum. 74 (11) (2003) 4794–4798.
[27] H. Davoodi, M. Jouda, J.G. Korvink, N. MacKinnon, V. Badilita, Broadband and multi-resonant sensors for NMR, Prog. Nucl. Magn. Reson. Spectrosc. 112 (2019) 34–54.
[28] S. Eckel, J. Nagel, M. Jouda, J.G. Korvink, A.Ç. Ulusoy, Design of planar transmission line microwave probes for broadband EPR spectroscopy, J. Magn. Reson. 374 (2025) 107866.

[29] R. Narkowicz, D. Suter, I. Niemeyer, Scaling of sensitivity and efficiency in planar microresonators for electron spin resonance, Rev. Sci. Instrum. 79 (8) (2008).
[30] N. Dayan, Y. Ishay, Y. Artzi, D. Cristea, E. Reijerse, P. Kuppusamy, A. Blank, Advanced surface resonators for electron spin resonance of single microcrystals, Rev. Sci. Instrum. 89 (12) (2018).
[31] G. Joshi, R. Miller, L. Ogden, M. Kavand, S. Jamali, K. Ambal, S. Venkatesh, D. Schurig, H. Malissa, J.M. Lupton, et al., Separating hyperfine from spin-orbit interactions in organic semiconductors by multi-octave magnetic resonance using coplanar waveguide microresonators, Appl. Phys. Lett. 109 (10) (2016).
[32] W.R. Hagen, Broadband tunable electron paramagnetic resonance spectroscopy of dilute metal complexes, J. Phys. Chem. A 123 (32) (2019) 6986–6995.
[33] Y. Ishay, A. Blank, Optimization methods for the design of sensitive surface ESR resonators, Appl. Magn. Reson. 48 (2017) 1249–1262.
[34] S. Wadhwa, M. Jouda, Y. Deng, O. Nassar, D. Mager, J.G. Korvink, Topologically optimized magnetic lens for magnetic resonance applications, Magn. Reson. 1 (2) (2020) 225–236.
[35] K. Chau-Nguyen, V. Badilita, J.G. Korvink, Concept for a geometry-insensitive high-field magnetic resonance detector, Eng. Comput. (2024) 1–16.
[36] A. Dewandre, J. Rivero-Rodriguez, Y. Vitry, B. Sobac, B. Scheid, Microfluidic droplet generation based on non-embedded co-flow-focusing using 3D printed nozzle, Sci. Rep. 10 (1) (2020) 21616.
[37] D.J. Lurie, K. Mäder, Monitoring drug delivery processes by EPR and related techniques—principles and applications, Adv. Drug Deliv. Rev. 57 (8) (2005) 1171–1190.
[38] A. Lipovsky, Z. Tzitrinovich, H. Friedmann, G. Applerot, A. Gedanken, R. Lubart, EPR study of visible light-induced ROS generation by nanoparticles of ZnO, J. Phys. Chem. C 113 (36) (2009) 15997–16001.
[39] M. Solsona, J. Vollenbroek, C. Tregouet, A.-E. Nieuwelink, W. Olthuis, A. Van Den Berg, B. Weckhuysen, M. Odijk, Microfluidics and catalyst particles, Lab A Chip 19 (21) (2019) 3575–3601.
[40] T. Moragues, M. Agrachev, S. Mitchell, G. Jeschke, J. Pérez-Ramírez, A.J. Demello, Droplet-based EPR spectroscopy for real-time monitoring of liquid-phase catalytic reactions, Small Methods (2025) 2401771.
[41] C. Purser, V. Bhallamudi, C. Wolfe, H. Yusuf, B. McCullian, C. Jayaprakash, M. Flatté, P. Hammel, Broadband electron paramagnetic resonance spectroscopy in diverse field conditions using optically detected nitrogen-vacancy centers in diamond, J. Phys. D: Appl. Phys. 52 (30) (2019) 305004.